

# ACTIVE GALACTIC NUCLEI SELECTED FROM *GALEX* SPECTROSCOPY: THE IONIZING SOURCE SPECTRUM AT $Z \sim 1$ <sup>1,2</sup>

AMY J. BARGER,<sup>3,4,5</sup> BARGER@ASTRO.WISC.EDU LENNOX L. COWIE<sup>5</sup>

*In press at The Astrophysical Journal*

## ABSTRACT

We use a complete sample of Ly $\alpha$  emission-line selected active galactic nuclei (AGNs) obtained from nine deep blank fields observed with the grism spectrographs on the *Galaxy Evolution Explorer* (*GALEX*) satellite to measure the normalization and spectral shape of the AGN contribution to the ionizing background (rest-frame wavelengths 700-900 Å) at  $z \sim 1$ . Our sample consists of 139 sources selected in the redshift range  $z = 0.65 - 1.25$  in the near-ultraviolet (NUV; 2371 Å central wavelength) channel. The area covered is 8.2 deg<sup>2</sup> to a NUV magnitude of 20.5 (AB) and 0.92 deg<sup>2</sup> at the faintest magnitude limit of 21.8. The *GALEX* AGN luminosity function agrees well with those obtained using optical and X-ray AGN samples, and the measured redshift evolution of the ionizing volume emissivity is similar to that previously obtained by measuring the *GALEX* far-ultraviolet (FUV; 1528 Å central wavelength) magnitudes of an X-ray selected sample. For the first time we are able to construct the shape of the ionizing background at  $z \sim 1$  in a fully self-consistent way.

*Subject headings:* cosmology: observations — galaxies: active — galaxies: distances and redshifts — intergalactic medium

## 1. INTRODUCTION

An important parameter in the cosmological modeling of galaxies and the intergalactic gas is the ionizing background radiation produced by the overall population of active galactic nuclei (AGNs) and star-forming galaxies as a function of wavelength and redshift. Usually the input ionizing source spectrum for such models is computed by convolving an approximate quasar spectral energy distribution (SED) determined from composite quasar spectra with a quasar luminosity function determined from optical data (e.g., Haardt & Madau 1996; Madau et al. 1999; Haardt & Madau 2001; Meiksin 2005; Siana et al. 2008; Dall’aglio et al. 2009). (Note that Gilmore et al. 2009 adopted the Hopkins et al. 2007 quasar luminosity function, which tries to take into account obscured sources, but obscured sources will not contribute to the ionizing background.) However, using optical quasar luminosity functions that have been extrapolated beyond where they have been measured (especially if the turn-over has not been observed) can result in overestimates of the ionizing background. X-ray luminosity functions, which probe to fainter luminosities

(e.g., Barger et al. 2005; Richards et al. 2005), provide a better approach (Cowie et al. 2009; hereafter, CBT09).

In CBT09 we measured the ionizing fluxes from a wide-field (0.9 deg<sup>2</sup>) X-ray sample with optical and UV imaging observations and found that the AGN contribution to the ionizing background peaks at  $z \sim 2$ . These results are lower than previous estimates of the AGN contribution, confirming that ionization from AGNs is insufficient to maintain the observed ionization of the intergalactic medium (IGM) at  $z > 3$  (see Bolton et al. 2005 and Meiksin 2005 for earlier estimates that suggested this result).

Ideally, however, one would like a direct measurement of the shape of the input ionizing source spectrum. Fortunately, with the advent of the *Galaxy Evolution Explorer* (*GALEX*) satellite (Martin et al. 2005), this is now possible at  $z \sim 1$ . Obtaining the shape of this spectrum is the primary goal of the present paper. We use *GALEX* grism spectroscopic observations to measure the AGN contribution to the ionizing background at  $z \sim 1$  directly from the UV spectra. For this we use the Ly $\alpha$  selected sample from Cowie et al. (2010; hereafter, CBH10), which should provide an essentially complete sample of broad-line AGNs (BLAGNs) and a nearly complete sample of all AGNs contributing to the ionizing flux in the redshift interval  $z = 0.65 - 1.25$ . We then go a step further and measure the ionizing source spectrum at rest-frame wavelengths 700 – 900 Å. We note, however, that this wavelength coverage is insufficient to characterize the full Lyman continuum background.

The outline of the paper is as follows. In Section 2 we briefly describe the 139  $z = 0.65 - 1.25$  sources in the CBH10 sample. In Section 3 we test the completeness of the sample by comparing with an X-ray selected AGN sample in the same redshift interval. In Section 4 we construct the rest-frame UV (1450 Å) luminosity function and compare it with the UV luminosity functions derived from X-ray and optically selected samples in the

<sup>1</sup> Based in part on data obtained from the Multimission Archive at the Space Telescope Science Institute (MAST). STScI is operated by the Association of Universities for Research in Astronomy, Inc., under NASA contract NAS5-26555. Support for MAST for non-*HST* data is provided by the NASA Office of Space Science via grant NAG5-7584 and by other grants and contracts.

<sup>2</sup> Based in part on data obtained at the W. M. Keck Observatory, which is operated as a scientific partnership among the California Institute of Technology, the University of California, and NASA and was made possible by the generous financial support of the W. M. Keck Foundation.

<sup>3</sup> Department of Astronomy, University of Wisconsin-Madison, 475 North Charter Street, Madison, WI 53706.

<sup>4</sup> Department of Physics and Astronomy, University of Hawaii, 2505 Correa Road, Honolulu, HI 96822.

<sup>5</sup> Institute for Astronomy, University of Hawaii, 2680 Woodlawn Drive, Honolulu, HI 96822.

same redshift interval. In Section 5 we determine the ionizing source spectrum at  $z \sim 1$  and show that the normalization agrees well with recent determinations at this redshift. In Section 6 we compute the shape of the comoving volume emissivity (after correcting for incompleteness and for the effects of Lyman scattering and absorption in the intervening intergalactic medium) versus rest-frame wavelength for the redshift intervals  $z = 0.65 - 0.95$  and  $z = 0.95 - 1.25$ . In Section 7 we summarize our results.

We use a standard  $H_0 = 70 \text{ km s}^{-1} \text{ Mpc}^{-1}$ ,  $\Omega_m = 0.3$ , and  $\Omega_\Lambda = 0.7$  cosmology throughout. All magnitudes are given in the AB magnitude system, where an AB magnitude is defined by  $m_{AB} = -2.5 \log f_\nu - 48.60$ . Here  $f_\nu$  is the flux of the source in units of  $\text{erg cm}^{-2} \text{ s}^{-1} \text{ Hz}^{-1}$

## 2. THE GALEX SAMPLE

CBH10 constructed a sample of 139 Ly $\alpha$  emission line-selected sources in the redshift interval  $z = 0.65 - 1.25$  from nine blank high galactic latitude fields with the deepest GALEX grism observations. They took the near-UV (NUV) and far-UV (FUV) extracted spectra and the NUV magnitudes from the Multimission Archive at STScI (MAST). Morrissey et al. (2007) detail the spectral extraction techniques used by the GALEX team in analyzing the grism data and discuss the UV spectra and magnitudes. We summarize the fields in Table 1, where we give in column (1) the GALEX name, in columns (2) and (3) the J2000 right ascension and declination, in column (4) the exposure time in kiloseconds, in column (5) the limiting NUV magnitude to which the spectra were extracted, in column (6) the galactic  $E(B - V)$  in the direction of the field from Schlegel et al. (1998), in column (7) the galactic latitude, in column (8) the number of sources with spectra lying within a radius of 32'.5 from the field center (chosen because in the outermost regions of the fields there is a higher fraction of poor quality spectra), and in column (9) the number of these sources found to have a Ly $\alpha$  emission line in the redshift range  $z = 0.65 - 1.25$  based on their NUV spectra. The extracted sources per field constitute nearly complete samples to the NUV limiting magnitudes given in the table (i.e., these are NUV selected samples and comprise both galaxies and a significant number of stars). The FUV spectra cover a wavelength range of  $\sim 1300 - 1800 \text{ \AA}$  at a resolution of  $\sim 10 \text{ \AA}$ , and the NUV spectra cover a wavelength range of  $\sim 1850 - 3000 \text{ \AA}$  at a resolution of  $\sim 25 \text{ \AA}$ .

Each of the spectra was corrected for the Milky Way extinction in the field using the Schlegel et al. (1998) extinction and the Cardelli et al. (1989) reddening law. Because the Galactic extinction towards these fields is very low (Table 1), the net effect is extremely small. On average the shape of the spectra is nearly unchanged and the normalization is raised by a factor of 1.08. The low extinctions in the present sample represent a considerable advantage over random quasar samples where the extinction for many of the objects will be high.

CBH10 determined the observed area as a function of NUV magnitude for each field by computing the ratio of sources with GALEX spectra at a given NUV magnitude to sources with that NUV magnitude in the continuum catalog. They multiplied this ratio for each field by the area corresponding to the 32'.5 selection radius

and summed the results for the 9 fields to form an area-magnitude relation (their Figure 4(c)). The area is the  $8.2 \text{ deg}^2$  area of the 9 fields for magnitudes brighter than NUV = 20.5 and then drops as the limiting magnitudes of each of the individual fields is reached. It falls to zero at  $\sim 21.8$ , which is the limiting depth of the deepest (GROTH 00) field.

CBH10 describe their search procedure for finding emission lines in the GALEX spectra. Because the spectra become very noisy at the edges of the wavelength ranges, they restricted their higher redshift search to the redshift interval  $z = 0.65 - 1.25$  corresponding to the wavelength range 2006–2736  $\text{\AA}$  in the NUV spectrum for the Ly $\alpha$  emission line. They measured redshifts for each source with an emission line in this wavelength range and split the sources into either an AGN class (if there were high-excitation lines; usually OVI, NV, or CIV would be present in addition to the Ly $\alpha$  line) or a candidate Galaxy class (if there were only a single line visible; in this case the line was assumed to be Ly $\alpha$  for determining a redshift, which they showed was an extremely reliable assumption). CBH10 found that nearly all of the more luminous sources are AGNs (their Figures 4(a) and 4(b)), leaving relatively few candidate Galaxies in the redshift interval  $z = 0.65 - 1.25$  (see also Deharveng et al. 2008). Of these, many were detected in the FUV (their Figure 4(b)), suggesting that they are AGNs, too, since  $z \sim 1$  galaxies should be very faint or undetected in the FUV band, which lies below the Lyman continuum edge at these redshifts (e.g., Siana et al. 2007; CBT09). We shall hereafter refer to all of the sources that were not classified as AGNs as unclassified sources. Since nearly all of them are likely AGNs, we will refer to the combined AGN plus unclassified source sample as our “full” AGN sample. We note that we have confirmed four of the unclassified sources as star formers through optical spectroscopic observations, but excluding them from our analysis makes no difference to the results.

## 3. TESTING THE COMPLETENESS OF THE GALEX AGN SAMPLE

We test the completeness of the GALEX AGN sample by comparing with an X-ray selected AGN sample in the same redshift interval. In Figure 1 we show the number counts for the GALEX AGN sample (black squares) and for the GALEX full AGN sample (blue triangles) versus NUV magnitude in the redshift interval  $z = 0.65 - 1.25$ . (There is only a very small difference between the AGN and the full AGN results.) In each magnitude bin the counts are the sum of the inverse areas for all the sources in that bin. The error bars are  $\pm 1\sigma$  based on the Poisson errors corresponding to the number of sources in each bin. The number counts per square degree per unit magnitude,  $N$ , are well described by the form (blue dashed line)

$$\log N = 0.40 (\text{NUV} - 18.4) \quad (1)$$

to the limiting NUV magnitude of the grism data of 21.8. This functional form implies an equal amount of light in each magnitude interval.

For the X-ray selected AGN sample in the same redshift interval we use the extremely spectroscopically complete Chandra samples of Trouille et al. (2008, 2009) and

TABLE 1  
GALEX FIELDS

Name	R.A. (J2000.0)	Decl. (J2000.0)	Exp. (ks)	NUV <sub>lim</sub> (mag)	$E(B - V)$	Gal. Lat. (deg)	No. w/sp. ( $< 32!5$ )	No. w/Ly $\alpha$
(1)	(2)	(3)	(4)	(5)	(6)	(7)	(8)	(9)
GROTH 00	214.99182	52.78173	291	21.8	0.007	59.5	1152	61
NGPDWS 00	219.15610	35.17135	156	21.5	0.009	66.2	738	39
CDFS 00	53.12779	-27.87137	149	21.5	0.008	-54.4	876	36
COSMOS 00	150.11900	2.20583	140	21.5	0.018	42.1	779	27
ELAISS1 00	9.63857	-43.99023	84	21.2	0.007	-72.9	589	17
SIRTF00	259.12387	59.90915	80	21.2	0.020	35.0	800	21
LOCK 00	162.67843	58.73117	48	20.9	0.009	52.1	390	10
SIRTF01	260.41425	59.34286	34	20.7	0.029	34.4	612	14
HDFN 00	189.20946	62.19772	24	20.5	0.012	54.8	265	10

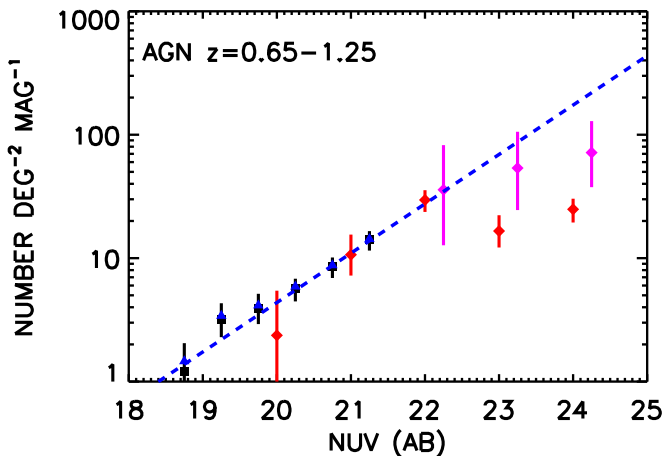


FIG. 1.— Number counts of the *GALEX* AGNs in the redshift interval  $z = 0.65 - 1.25$  vs. NUV magnitude (black squares with  $1\sigma$  errors based on the number of sources in each bin). The blue triangles show the values if we also include the unclassified sources in this redshift interval. For comparison, we show the number counts of an X-ray selected sample in a  $0.9 \text{ deg}^2$  area (the CLANS and CLASXS fields) with red diamonds and in a smaller but much deeper  $200 \text{ arcmin}^2$  area (the CDF-N) with purple diamonds. Over the magnitude range of the *GALEX* grism data the *GALEX* AGN number counts agree well with the X-ray selected AGN number counts and are well fit with a slope of 0.4 (blue dashed line). Thus, each magnitude bin contains roughly equal light density.

references therein on the *Chandra* Large-Area Synoptic X-ray Survey (CLASXS), the *Chandra* Lockman Area North Survey (CLANS), and the *Chandra* Deep Field-North (CDF-N). Essentially all of the X-ray sources in the redshift interval  $z = 0.65 - 1.25$  are expected to be identified.

The CLASXS and CLANS fields are covered by a number of *GALEX* pointings, all of which are roughly 30 ks in depth. The CDF-N *GALEX* exposures are 165 ks in the NUV and 96 ks in the FUV. CBT09 describe how the *GALEX* magnitudes for the sources in the X-ray samples were measured. In brief, given the large point-spread function (PSF) of *GALEX* ( $4!5 - 6!0$  FWHM), they used an  $8!''$  diameter aperture to measure the magnitudes using the *GALEX* zeropoints from Morrissey et al. (2007), and they corrected these to approximate total magnitudes using an offset that they determined to be  $-0.41$ . They measured the noise level in the images by randomly positioning apertures on blank regions of sky and mea-

suring the dispersion. In the CLASXS and CLANS fields they found the  $1\sigma$  limits to be slightly variable but typically about 26.1 in the NUV images and 26.5 in the FUV images. In the CDF-N field they found  $1\sigma$  limits of 26.8 in the NUV image and 27.4 in the FUV image. Only a small fraction ( $\sim 4\%$ ) of the X-ray sources in the CLASXS or CLANS fields are not covered by one of the *GALEX* pointings, and all of the CDF-N sources are covered. CBT09 only eliminated four sources where visual inspection showed that there was contamination from a nearby brighter *GALEX* source at the same wavelength. The X-ray sources themselves are so sparse that contamination by another X-ray source may be neglected.

In Figure 1 we show separately the number counts from the shallower CLASXS and CLANS fields (red diamonds), where the  $2 - 8 \text{ keV}$  flux limit is  $\sim 7 \times 10^{-15} \text{ erg cm}^{-2} \text{ s}^{-1}$  and the area is  $\sim 0.9 \text{ deg}^2$ , and the number counts from the CDF-N (purple diamonds), which is about 50 times deeper but has a much smaller area of  $\sim 200 \text{ arcmin}^2$ . Over the magnitude range of the *GALEX* grism data the *GALEX* AGN number counts agree extremely well with the CLASXS and CLANS AGN number counts. When we compare the NUV counts from the shallower X-ray fields with those from the CDF-N, we see that the former are becoming incomplete fainter than  $\text{NUV} \sim 22.5$ . The CDF-N number counts themselves should be complete to several magnitudes fainter than this, so their behavior suggests that the AGN number counts begin to turn down from the 0.4 slope at  $\text{NUV} \sim 23.5$ . This in turn suggests that the *GALEX* AGN sample measures a large fraction of the total NUV light at these redshifts.

#### 4. THE AGN LUMINOSITY FUNCTION

We next computed the binned rest-frame UV ( $1450 \text{ \AA}$ ) luminosity function for the *GALEX* full AGN sample using the NUV-continuum magnitudes and the  $1/V$  method (Felten 1976). We made the small differential  $K$ -corrections to  $1450 \text{ \AA}$  by assuming a quasar spectral energy distribution (SED) with  $f_\nu \sim \nu^{-0.44}$  (Vanden Berk et al. 2001). We show this luminosity function with black squares in Figure 2. The error bars are  $\pm 1\sigma$  based on the Poisson errors corresponding to the number of sources in each bin. We compare with the  $1450 \text{ \AA}$  luminosity function derived from the X-ray selected BLAGN luminosity function of Yencho et al. (2009) (red diamonds). For the conversion of  $2 - 8 \text{ keV}$  luminosity

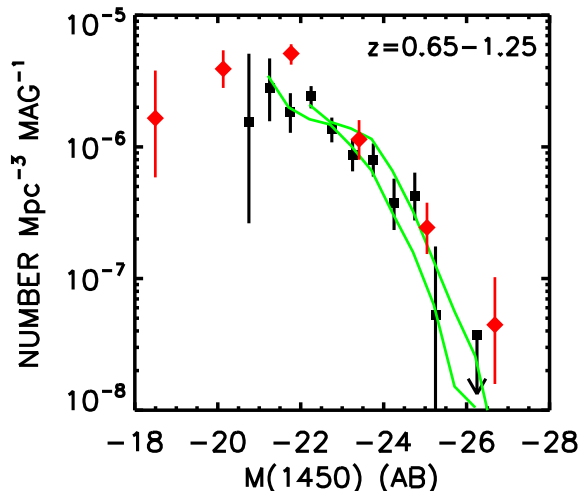


FIG. 2.— The rest-frame UV (1450 Å) luminosity function of the *GALEX* full AGN sample in the redshift interval  $z = 0.65 - 1.25$  (black squares with  $1\sigma$  error bars from the observed number of sources in each bin). Red diamonds show the converted X-ray selected BLAGN luminosity function in the same redshift interval from Yencho et al. (2009). The green curves (lower for  $z = 0.68 - 0.95$ ; upper for  $z = 0.95 - 1.25$ ) show the converted optically selected luminosity functions from Croom et al. (2004).

( $L_X$ ) to 1450 Å absolute magnitude we used the relation  $\nu L_\nu(2300 \text{ Å})/L_X = 7.46 \times (L_X/10^{44} \text{ erg s}^{-1})^{0.31}$  from CBT09, which is similar to previous work (e.g., Vignali et al. 2003). We again made the small differential  $K$ -corrections to 1450 Å by assuming  $f_\nu \sim \nu^{-0.44}$ . Finally, we compare with the optically selected quasar luminosity function of Croom et al. (2004) (green curves) scaled to 1450 Å by assuming  $f_\nu \sim \nu^{-0.44}$ . A similar result is obtained using the Richards et al. (2005) luminosity function.

The *GALEX* luminosity function agrees extremely well with these other determinations and reaches about a magnitude fainter than the wide-field optical samples used in the Croom et al. (2004) measurement. The X-ray-determined luminosity function from Yencho et al. (2009) is deeper yet and shows a turn-down at fainter magnitudes. This means that the UV light density is nearly convergent in the *GALEX* full AGN sample at these redshifts. If we extrapolate the *GALEX* luminosity function with a constant value below  $M(1450)_{\text{AB}} = -22$ , then the additional UV light density at magnitudes fainter than  $M(1450)_{\text{AB}} = -22$  is only 24% of the total light for the observed sources with magnitudes brighter than this value.

##### 5. THE IONIZING SPECTRUM OF $Z \sim 1$ AGNS

We next compared the flux measured from the spectra at rest-frame wavelengths both above and below the Lyman continuum break with the selection NUV magnitude. In Figure 3 we show the observed flux from the *GALEX* spectra at rest-frame (a) 800 – 880 Å (for  $z = 0.65 - 1.15$  only; note that we use only the portion of the wavelength range that is covered by the *GALEX* FUV spectra) and (b) 1400 – 1500 Å (for  $z = 0.65 - 0.95$  only, in order for the *GALEX* NUV spectra to cover the rest-frame wavelengths) versus NUV. The tight relation in (b) simply reflects the fact that the redshifted

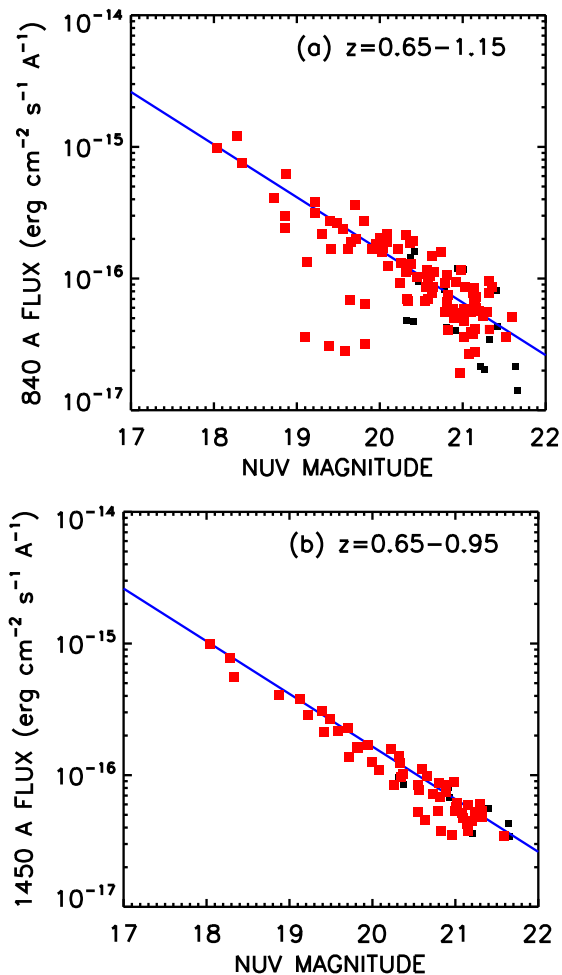


FIG. 3.— (a) Observed flux from the *GALEX* spectra at rest-frame 800 – 880 Å vs. NUV magnitude for sources in the redshift interval  $z = 0.65 - 1.15$ . Red squares denote sources classified as AGNs due to the presence of high-excitation lines, while black squares show the unclassified sources in this redshift interval. The blue line shows a linear fit to the data. (b) Same as (a) but for rest-frame 1400 – 1500 Å and restricted to  $z = 0.65 - 0.95$ , where the *GALEX* NUV spectra cover the rest-frame wavelengths. The blue line shows the expected value of the flux determined from the NUV continuum magnitude, since redshifted 1400 – 1500 Å matches closely to the NUV wavelength. There is a very small multiplicative factor (0.95) between the flux measured from the spectra and the flux measured from the broadband magnitudes.

1400 – 1500 Å spectral interval matches closely to the NUV wavelength. The data provide a test of the *GALEX* spectral intensity calibration, which appears to be extremely accurate, since the spectral fluxes differ by less than 5% from the broadband continuum fluxes.

As can be seen from Figure 3(a), most of the sources also obey a linear relation between the spectral flux at wavelengths just below the continuum break and the NUV flux. At 840 Å we find

$$f_\lambda(840 \text{ Å}) = 1.65 \times 10^{-16} 10^{-0.4(\text{NUV}-20)}, \quad (2)$$

where  $f_\lambda(840 \text{ Å})$  is the average spectral flux of the sources at rest-frame 800 – 880 Å in  $\text{erg cm}^{-2} \text{ s}^{-1} \text{ Å}^{-1}$ . We show this as the blue line in Figure 3(a). A small fraction of the sources (i.e., those where there is a significant continuum break) lie significantly below this relation. The mean  $f_\lambda$

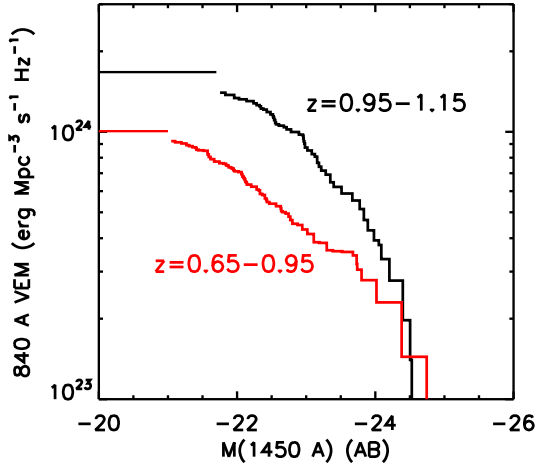


FIG. 4.— Cumulative comoving volume emissivity (VEM) for the full AGN sample at rest-frame 840 Å vs. rest-frame 1450 Å absolute magnitude for the two redshift intervals  $z = 0.65 - 0.95$  (red curve) and  $z = 0.95 - 1.15$  (black curve). The horizontal lines show the incompleteness corrected values for the two redshift intervals.

ratio,  $f_\lambda(840 \text{ \AA})/f_\lambda(1450 \text{ \AA})$ , is 1.11; the mean  $f_\nu$  ratio is 0.37. CBT09 gave an  $f_\nu$  ratio of 0.26 between 912 Å and 2300 Å, which for  $f_\nu \sim \nu^{-0.44}$  (Vanden Berk et al. 2001) would correspond to 0.34 for the  $f_\nu(840 \text{ \AA})/f_\nu(1450 \text{ \AA})$  ratio, in close agreement with the present value.

We then computed the comoving volume emissivity (VEM) in the rest-frame wavelength range 800 – 880 Å using the  $1/V$  methodology. In Figure 4 we show the cumulative contribution to the VEM as a function of the rest-frame 1450 Å absolute magnitude for the redshift intervals  $z = 0.65 - 0.95$  and  $z = 0.95 - 1.15$ , which reach  $M_{\text{AB}}(1450 \text{ \AA}) \sim -21$  and  $\sim -21.7$ , respectively.

We have taken a simple approach to estimate the incompleteness correction due to sources fainter than our selection NUV magnitude limit. As a result of the two linear relations in Figure 3, the  $f_\lambda(840 \text{ \AA})/f_\lambda(1450 \text{ \AA})$  ratio stays fixed over the NUV magnitude range of our sources, which implies that the spectral shape is invariant over that magnitude range. If we assume that the ratio also remains fixed at fainter magnitudes, then any estimate of the incompleteness correction made at 1450 Å can be applied at any other wavelength.

In order to estimate the incompleteness correction at 1450 Å, we used the form of the 1450 Å luminosity function (e.g., Figure 2). We determined the amount of missing light at 1450 Å by assuming a constant value per  $\text{Mpc}^3$  per mag below the limiting absolute magnitude that we measured. From the ratio of this integral to the integral made only to the limiting absolute magnitude, we obtained correction factors of 1.09 ( $z = 0.65 - 0.95$ ) and 1.24 ( $z = 0.95 - 1.15$ ). We applied these corrections to the measured 840 Å VEMs, giving incompleteness corrected values that are not substantially higher than the direct measurements (horizontal lines in Figure 4). Numerically these values are  $1.07 \pm 0.19 \times 10^{24} \text{ erg Mpc}^{-3} \text{ s}^{-1}$  at  $z = 0.8$  and  $1.68 \pm 0.23 \times 10^{24} \text{ erg Mpc}^{-3} \text{ s}^{-1}$  at  $z = 1.05$ .

We can compare these results to CBT09’s determina-

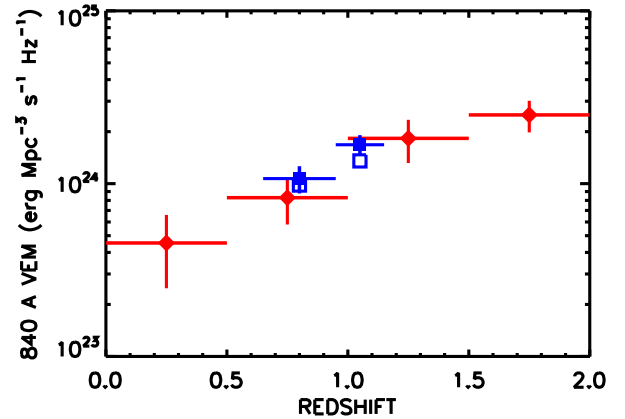


FIG. 5.— Evolution of the comoving volume emissivity at rest-frame 840 Å vs. redshift for the redshift intervals  $z = 0.65 - 0.95$  and  $z = 0.95 - 1.15$  (blue open squares show the directly measured values, and solid squares show the incompleteness corrected values). We also show the evolution determined by CBT09 from measuring the *GALEX* FUV magnitudes of an X-ray selected sample (red diamonds). For each point the  $x$ -axis error bars show the redshift interval and the  $y$ -axis error bars show the  $1\sigma$  error computed using the jackknife method.

tion of the redshift evolution of the VEM just below the Lyman continuum edge. In Figure 5 we show CBT09’s X-ray based points with red diamonds and the present points with blue squares (open for directly measured values; solid for incompleteness corrected values). The  $1\sigma$  errors for both samples have been computed with the jackknife method. The smaller error bars on the present points reflect the much larger area sampled by the *GALEX* images than by the X-ray images. It is very reassuring that the two samples agree within the formal errors.

## 6. THE SHAPE OF THE SPECTRUM

With the grism data we are able to move one critical step beyond CBT09 and compute the shape of the VEM with wavelength. As discussed in Section 1, a direct measurement of the shape of the input ionizing source spectrum is ideally required for the cosmological modeling of galaxies and the intergalactic gas. For each rest-frame wavelength interval we computed the VEM using the same procedure that we used for the rest-frame 800 – 880 Å interval, including applying at all wavelengths the incompleteness corrections of 1.09 and 1.24, respectively, for the low and high-redshift intervals. However, in order to obtain the true rest-frame VEM spectrum, we also need to correct for the effects of the Lyman scattering and absorption in the intervening intergalactic medium (Møller & Jakobsen 1990; Haardt & Madau 1996; Fardal et al. 1998). While this correction is not large at  $z = 1$ , it does slightly steepen the spectral slope in the extreme UV (EUV) and raise the normalization.

The effects of the intergalactic medium (IGM) may be separated into scattering by the Ly $\alpha$  forest lines below a rest-frame of 1216 Å and photoelectric absorption from the Lyman continuum of hydrogen below 912 Å. At the wavelengths of interest we may neglect helium. The effects of the forest are dominated by systems with

column densities around  $10^{14} \text{ cm}^{-2}$ , where Ly $\alpha$  lines saturate, while the photoelectric absorption is dominated by systems with column densities  $\sim 10^{17} \text{ cm}^{-2}$ , where the Lyman continuum edge saturates.

The decrement in the Ly $\alpha$ -only portion of the forest has been directly measured by Kirkman et al. (2007). They obtained a value of  $0.037 \times (1+z)^{1.1}$  at these redshifts. The redshift dependence, which causes less light to be absorbed at shorter wavelengths (i.e., because there are fewer systems at lower redshifts), is roughly balanced by the onset of absorption by the higher Lyman series lines at shorter wavelengths, resulting in a roughly constant reduction as a function of wavelength near  $z = 1$  (see Figure 6a of Inoue & Iwata 2008).

The photoelectric absorption is most directly related to the density of Lyman limit systems (LLSs). In LLSs the optical depth,  $\tau$ , at the Lyman continuum edge exceeds one. The surface density of LLSs at these redshifts has recently been remeasured by Songaila & Cowie (2010). They found that the number density per unit redshift evolves as  $0.15 \times (1+z)^{1.9}$ . This normalization is slightly lower than previous measurements at these redshifts (Stengler-Larrea et al. 1995). We may use this normalization in conjunction with the distribution of the number of systems as a function of the neutral hydrogen column density to compute the complete photoelectric effect. The column density distribution is usually parameterized as a power law or broken power law function of the column density. Inoue & Iwata (2008) assumed a broken power law with a slope of  $-1.6$  below the Lyman limit and  $-1.3$  above (e.g., Janknecht et al. 2006; Songaila & Cowie 2010), which we adopt here. We have also computed the correction for a single power law with a slope of  $-1.4$  in the vicinity of the Lyman limit (Misawa et al. 2007) to investigate the sensitivity to the assumed column density distribution. This slightly decreases the correction, but the changes produced are smaller than the statistical errors for both the normalization and the spectral slope.

We have used these values to make Monte Carlo estimates of the photoelectric absorption (Bershady et al. 1999; Inoue & Iwata 2008). In Figure 6 we show the photoelectric absorption decrements that we obtained at (a)  $z = 0.8$  and (b)  $z = 1.1$  from averaging (in each case) 1000 lines of sight. We show the values obtained both from using only systems with optical depths less than one at the Lyman edge (dashed line) and from using all the systems regardless of their optical depths (solid line). The Monte Carlo simulations also allow us to estimate the uncertainty introduced by the finite number of systems we are observing. For the case where we used all the systems regardless of their optical depth, we also show with dotted lines the range of corrections that we found in 20 computations using only 60 lines of sight (which is roughly equal to the number of lines of sight in the present sample; we have 53 systems at  $z = 0.65 - 0.95$  and 63 at  $z = 0.95 - 1.25$ ). At the shorter wavelengths this corresponds to about a 10% uncertainty in the correction. The large range is a consequence of the small number of systems which contribute to the opacity at  $\tau > 1$ . The uncertainty in the correction for the  $\tau < 1$  systems only is much smaller (about 3% or less). This is because there is a much larger number of low column

density systems, and hence the correction is better averaged even in a small number of lines of sight.

We have applied the correction in two ways. In the first we excluded the small number of quasars with measured LLSs in their spectra using the list in Songaila & Cowie (2010). We corrected for the missing light from these AGNs by proportionally reducing the observed area. We then used the  $\tau < 1$  correction to compute the final VEM. In Figure 7(a) we show the VEM corrected in this way and its  $1\sigma$  errors in the redshift intervals  $z = 0.65 - 0.95$  (red squares) and  $z = 0.95 - 1.25$  (blue diamonds) versus wavelength. The advantage of this method is that it minimizes the correction and also avoids the statistical uncertainties in the  $\tau > 1$  correction. However, we may fail to identify LLSs in the fainter and noisier spectra. We have therefore also computed the VEM from the full quasar sample (i.e., not excluding systems with LLSs). In this case we apply the full correction, including the opacity from the  $\tau > 1$  systems. In Figure 7(b) we show the VEM corrected in this way and its  $1\sigma$  errors in the same redshift intervals. We summarize the values that we derived using both methods in Table 2.

Scott et al. (2004) fitted a single power law to their composite EUV QSO spectrum from *Far-Ultraviolet Spectroscopic Explorer (FUSE)* data, but both Zheng et al. (1997) and Telfer et al. (2002) used a broken power law to fit their composite EUV QSO spectra from *Hubble Space Telescope (HST)* data. For each redshift interval we have fitted a broken power law to the data, excluding the bins at 775 Å, 1025 Å, and 1225 Å to exclude the strong emission lines in the spectra. The position of the break is quite uncertain. We have chosen to position it at 1225 Å. We show the fits as straight lines in Figure 7 for each case. Although it is possible that there is more structure within the error bars, the present data do not justify a more complicated fit. We present this simple parameterization in order to provide quantitative numbers for use by others. Since the differences between the two methods lie within the statistical errors (see Table 2), we consider only the cases with the LLSs excluded (Figure 7a), which should be more robust. For  $z = 0.65 - 0.95$  we obtain

$$\log(\text{VEM}) = (24.11 \pm 0.03) + (1.76 \pm 0.25) \log(w/800 \text{ \AA}) \quad (3)$$

below 1225 Å and

$$\log(\text{VEM}) = (24.46 \pm 0.01) + (0.36 \pm 0.45) \log(w/1250 \text{ \AA}) \quad (4)$$

above 1225 Å. For  $z = 0.95 - 1.25$  we obtain

$$\log(\text{VEM}) = (24.34 \pm 0.02) + (2.01 \pm 0.20) \log(w/800 \text{ \AA}) \quad (5)$$

below 1225 Å and

$$\log(\text{VEM}) = (24.69 \pm 0.02) - (0.51 \pm 0.97) \log(w/1250 \text{ \AA}) \quad (6)$$

above 1225 Å. In all of the above equations,  $w$  is the rest-frame wavelength.

The slopes are consistent between the two redshift ranges within the statistical errors, while the normalization rises by 0.23 dex or a factor of 1.7. The short wavelength slope is considerably steeper than the value of 0.56 ( $-0.28, 0.38$ ) derived by Scott et al. (2004) but agrees well with the values of  $1.76 \pm 0.12$  derived by Telfer

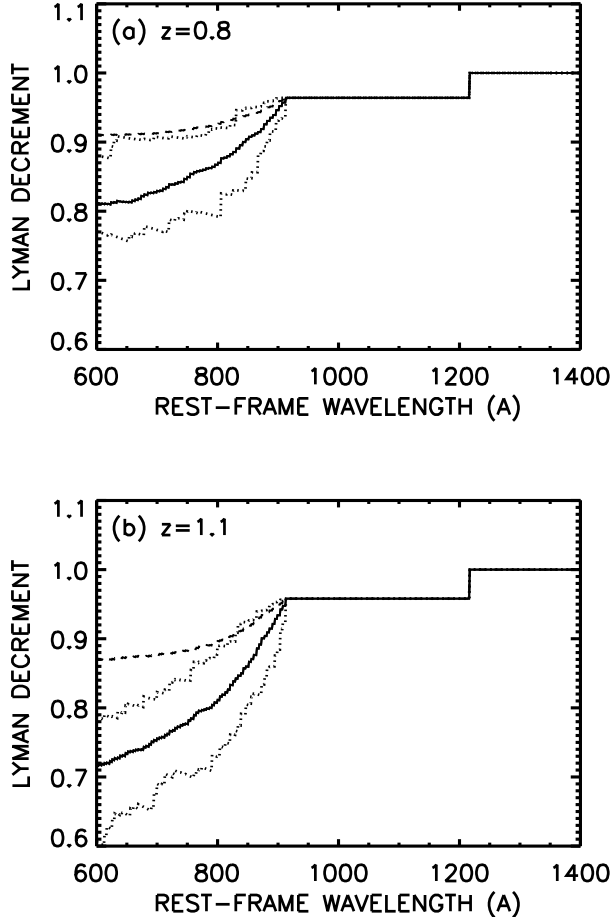


FIG. 6.— Monte Carlo estimates of the photoelectric absorption decrements at (a)  $z = 0.8$  and (b)  $z = 1.1$  obtained from averaging (in each case) 1000 lines of sight. The dashed curves only show the values from systems with optical depths less than one at the Lyman edge, while the solid curves show the values from all systems regardless of their optical depths. The dotted curves show the range of corrections for 20 computations of only 60 lines of sight, which is similar to the number of systems that we have in each redshift interval.

et al. (2002) and  $1.96 \pm 0.15$  derived by Zheng et al. (1997). These various samples have different luminosities and redshift selections, which may account for some part of the differences. The present sample is properly weighted over the sources contributing to the ionizing background.

## 7. SUMMARY

We used a complete sample of Ly $\alpha$  emission-line selected AGNs obtained from nine deep blank fields observed with the grism spectrographs on *GALEX* to measure the AGN contribution to the ionizing background at  $z \sim 1$ . We found that the *GALEX* AGN luminosity function is in good agreement with luminosity functions obtained from optical and X-ray AGN samples. We also found that our measurements of the 840 Å VEM at  $z = 0.8$  and  $z = 1.05$  agree within the formal errors with the redshift evolution of the comoving volume emissivity determined by CBT09 using an X-ray selected AGN sample. Finally, for the first time, we were able to compute

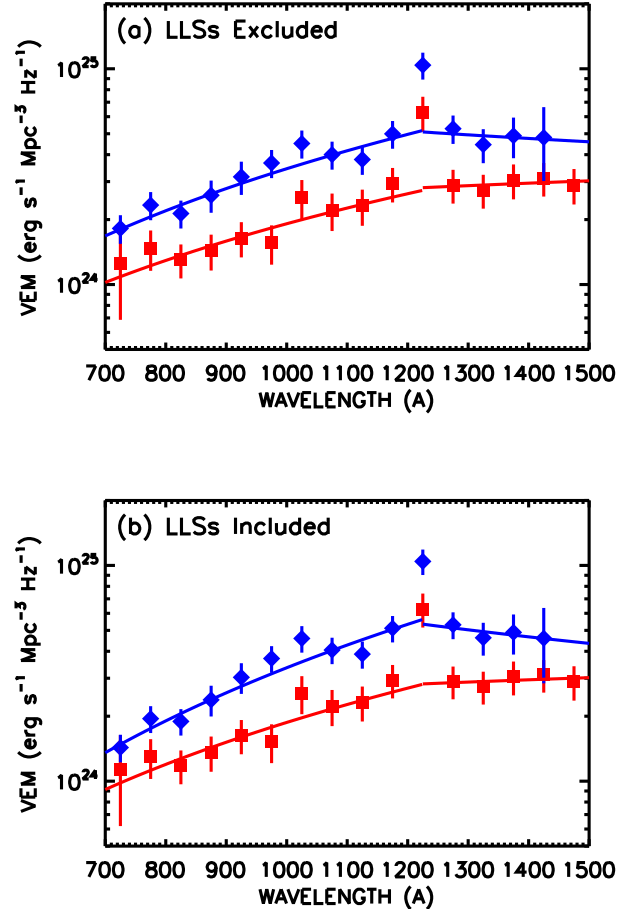


FIG. 7.— Shape of the comoving volume emissivity vs. rest-frame wavelength for the redshift intervals  $z = 0.65 - 0.95$  (red squares) and  $z = 0.95 - 1.25$  (blue diamonds). The values shown are corrected for incompleteness, and the error bars are  $\pm 1 \sigma$  computed using the jackknife method. In (a) we exclude the quasars with measured LLSs in their spectra before applying the  $\tau < 1$  correction to compute the final VEM. In (b) we use the full quasar sample and apply the full correction, including the opacity from the  $\tau > 1$  systems, to compute the final VEM. The straight lines show broken power law fits.

directly the shape of the VEM with wavelength for the redshift intervals  $z = 0.65 - 0.95$  and  $z = 0.95 - 1.25$ . We corrected both for incompleteness and for the effects of the Lyman scattering and absorption in the intervening intergalactic medium. The slopes are consistent between the two redshift ranges within the statistical errors, while the normalization rises by a factor of 1.7. At  $< 1125$  Å our slope is considerably steeper than that determined by Scott et al. (2004) using *FUSE* data, but it is in good agreement with the slopes determined by Telfer et al. (2002) and Zheng et al. (1997) using *HST* data.

We thank the anonymous referee for a helpful report. We gratefully acknowledge support from NSF grants AST-0708793 (A. J. B.) and AST-0709356 (L. L. C.), the University of Wisconsin Research Committee with funds granted by the Wisconsin Alumni Research Foundation, and the David and Lucile Packard Foundation

(A. J. B.).

## REFERENCES

- Barger, A. J., Cowie, L. L., Mushotzky, R. F., Yang, Y., Wang, W.-H., Steffen, A. T., & Capak, P. 2005, *AJ*, 129, 578
- Bershady, M. A., Charlton, J. C., & Geoffroy, J. M. 1999, *ApJ*, 518, 103
- Bolton, J. S., Haehnelt, M., Viel, M., & Springel, V. 2005, *MNRAS*, 307, 1178
- Cardelli, J. A., Clayton, G. C., & Mathis, J. S. 1989, *ApJ*, 345, 245
- Cowie, L. L., Barger, A. J., & Hu, E. M. 2010, *ApJ*, 711, 928 (CBH10)
- Cowie, L. L., Barger, A. J., & Trouille, L. 2009, *ApJ*, 692, 1476 (CBT09)
- Croom, S. M., Smith, R. J., Boyle, B. J., Shanks, T., Miller, L., Outram, P. J., & Loaring, N. S. 2004, *MNRAS*, 349, 1397
- Dall'aglio, A., Wisotzki, L., & Worseck, G. 2009, *ApJ*, submitted (arXiv0906.1484)
- Deharveng, J.-M. et al. 2008, *ApJ*, 680, 1072
- Fardal, M. A., Giroux, M. L., & Shull, J. M. 1998, *AJ*, 115, 2206
- Felten, J. E. 1976, *ApJ*, 207, 700
- Gilmore, R. C., Madau, P., Primack, J. R., Somerville, R. S., & Haardt, F. 2009, *MNRAS*, 399, 1694
- Haardt, F., & Madau, P. 1996, *ApJ*, 461, 20
- Haardt, F., & Madau, P. 2001, in *Clusters of Galaxies and the High Redshift Universe Observed in X-rays*, Eds. D. M. Neumann & J. T. T. Van, <http://moriond.in2p3.fr>
- Hopkins, P. F., Richards, G. T., & Hernquist, L. 2007, *ApJ*, 654, 731
- Inoue, A., K., & Iwata, I. 2008, *MNRAS*, 387, 1681
- Janknecht, E., Reimers, D., Lopez, S., & Tytler, D. 2006, *A&A*, 458, 427
- Kirkman, D., Tytler, D., Lubin, D., & Charlton, J. 2007, *MNRAS*, 376, 1227
- Madau, P., Haardt, F., & Rees, M. J. 1999, *ApJ*, 514, 648
- Martin, D. C., et al. 2005, *ApJ*, 619, L1
- Meiksin, A. 2005, *MNRAS*, 356, 596
- Misawa, T., Tytler, D., Iye, M., Kirkman, D., Suzuki, N., Lubin, D., & Kashikawa, N. 2007, *AJ*, 134, 1634
- Møller, P., & Jakobsen, P. 1990, *A&A*, 228, 299
- Morrissey, P., et al. 2007, *ApJS*, 173, 682
- Richards, G. T., et al. 2005, *MNRAS*, 360, 839
- Schlegel, D. J., Finkbeiner, D. P., & Davis, M. 1998, *ApJ*, 500, 525
- Scott, J. E., Kriss, G. A., Brotherton, M., Green, R. F., Hutchings, J., Shull, J. M., & Zheng, W. 2004, *ApJ*, 615, 135
- Siana, B., et al. 2007, *ApJ*, 668, 62
- Siana, B., et al. 2008, *ApJ*, 675, 49
- Songaila, A., & Cowie, L. L. 2010, *ApJ*, submitted
- Stengler-Larrea, E. A., et al. 1995, *ApJ*, 444, 64
- Telfer, R. C., Zheng, W., Kriss, G. A., & Davidsen, A. F. 2002, *ApJ*, 565, 773
- Trouille, L., Barger, A. J., Cowie, L. L., Yang, Y., & Mushotzky, R. F. 2008, *ApJS*, 179, 1
- Trouille, L., Barger, A. J., Cowie, L. L., Yang, Y., & Mushotzky, R. F. 2009, *ApJ*, 703, 2160
- Vanden Berk, D. E., et al. 2001, *AJ*, 122, 549
- Vignali, C., Brandt, W. N., & Schneider, D. P. 2003, *AJ*, 125, 433
- Yencho, B., Barger, A. J., Trouille, L., & Winter, L. M. 2009, *ApJ*, 698, 380
- Zheng, W., Kriss, G. A., Telfer, R. C., Grimes, J. P., & Davidsen, A. F. 1997, *ApJ*, 475, 469

TABLE 2  
VEM

Wavelength ( $\text{\AA}$ ) (1)	Raw VEM <sup>a</sup> (2)	Error <sup>a</sup> (3)	Lyman Corr. (4)	Final VEM (5)	Error (6)
LLSs Excluded, $z = 0.65 - 0.95$					
725	0.96	0.43	0.92	1.13	0.51
775	1.11	0.23	0.92	1.29	0.27
825	1.03	0.18	0.93	1.18	0.21
875	1.20	0.22	0.95	1.36	0.25
925	1.47	0.26	0.96	1.63	0.29
975	1.37	0.28	0.96	1.52	0.31
1025	2.30	0.46	0.96	2.56	0.51
1075	2.00	0.38	0.96	2.22	0.42
1125	2.09	0.39	0.96	2.32	0.43
1175	2.65	0.47	0.96	2.94	0.52
1225	5.87	1.05	1.00	6.28	1.13
1275	2.71	0.47	1.00	2.90	0.50
1325	2.56	0.44	1.00	2.74	0.48
1375	2.84	0.51	1.00	3.04	0.54
LLSs Excluded, $z = 0.95 - 1.25$					
725	1.01	0.15	0.88	1.43	0.21
775	1.39	0.20	0.89	1.95	0.28
825	1.37	0.19	0.90	1.89	0.27
875	1.78	0.29	0.93	2.38	0.39
925	2.32	0.38	0.96	3.03	0.49
975	2.84	0.40	0.96	3.70	0.52
1025	3.51	0.49	0.96	4.59	0.64
1075	3.11	0.44	0.96	4.05	0.57
1125	2.97	0.43	0.96	3.88	0.56
1175	3.92	0.55	0.96	5.11	0.72
1225	8.35	1.13	1.00	10.44	1.41
1275	4.24	0.60	1.00	5.31	0.76
1325	3.70	0.64	1.00	4.62	0.80
1375	3.92	0.82	1.00	4.89	1.03
LLSs Included, $z = 0.65 - 0.95$					
725	0.98	0.44	0.84	1.25	0.56
775	1.18	0.25	0.86	1.47	0.31
825	1.07	0.19	0.88	1.30	0.23
875	1.23	0.23	0.92	1.43	0.27
925	1.48	0.27	0.96	1.64	0.30
975	1.40	0.29	0.96	1.56	0.32
1025	2.27	0.47	0.96	2.52	0.53
1075	1.99	0.39	0.96	2.20	0.44
1125	2.08	0.40	0.96	2.31	0.44
1175	2.64	0.48	0.96	2.94	0.53
1225	5.85	1.08	1.00	6.26	1.16
1275	2.70	0.48	1.00	2.89	0.51
1325	2.56	0.46	1.00	2.74	0.49
1375	2.84	0.52	1.00	3.04	0.56
LLSs Included, $z = 0.95 - 1.25$					
725	1.11	0.17	0.77	1.82	0.28
775	1.49	0.22	0.80	2.33	0.35
825	1.42	0.21	0.83	2.13	0.32
875	1.87	0.32	0.90	2.59	0.44
925	2.42	0.42	0.96	3.16	0.55
975	2.80	0.42	0.96	3.66	0.55
1025	3.45	0.51	0.96	4.50	0.67
1075	3.07	0.45	0.96	4.00	0.59
1125	2.91	0.44	0.96	3.80	0.57
1175	3.83	0.56	0.96	4.99	0.73
1225	8.32	1.18	1.00	10.39	1.48
1275	4.22	0.64	1.00	5.28	0.79
1325	3.56	0.64	1.00	4.45	0.80
1375	3.92	0.84	1.00	4.89	1.04

<sup>a</sup> Raw values do not have the incompleteness correction or the Lyman correction. The VEM and errors are given in units of  $10^{24}$  erg Mpc<sup>-3</sup> s<sup>-1</sup> Hz<sup>-1</sup>.